Available online at www.sciencedirect.com
ScienceDirect
Journal of Solid State Chemistry 180 (2007) 3196–3210
JOURNAL OF SOLID STATE CHEMISTRY
www.elsevier.com/locate/jssc

Crystal structure, optical properties and colouring performance of karrooite $MgTi_2O_5$ ceramic pigments

Francesco Matteucci[a,*], Giuseppe Cruciani[b], Michele Dondi[a], Giorgio Gasparotto[c], David Maria Tobaldi[c,1]

[a]*ISTEC-CNR, Institute of Science and Technology for Ceramics, Via Granarolo 64, 48018 Faenza, Italy*
[b]*Department of Earth Sciences, University of Ferrara, Via Saragat 1, 44100 Ferrara, Italy*
[c]*Department of Earth and Geo-Environmental Sciences, University of Bologna, Piazza di Porta San Donato 1, 40126 Bologna, Italy*

Received 29 May 2007; received in revised form 7 August 2007; accepted 31 August 2007
Available online 11 September 2007

Abstract

Karrooite, $MgTi_2O_5$, is a promising ceramic pigment due to its high refractoriness and refractive indices, as well as its ability to host transition metal ions in two crystallographically distinct octahedral sites. The colouring performance was investigated combining X-ray powder diffraction with UV–vis–NIR spectroscopy on karrooite doped with V, Cr, Mn, Fe, Co or Ni (M) according to the formula $Mg_{1-x}Ti_{2-x}M_{2x}O_5$, with $x = 0.02$ and 0.05. Transition metals solubility in the karrooite lattice is not complete and a second phase is always present (geikielite or rutile). Structural data proved that incorporation of different chromophore ions into the karrooite structure affects unit cell parameters, bond length distances and angles, site occupancies and therefore cation order–disorder. Optical spectra exhibit broad absorbance bands of Co(II), Cr(IV), Fe(III), Mn(II), Mn(III), Ni(II), V(IV) with distinct contributions by cations in the M_1 and M_2 sites. Karrooite pigments have colours ranging from orange to brown-tan (Cr, Fe, Mn, V) to green (Co) and yellow (Ni) that are stable in low-temperature ($<1050\,^{\circ}C$) ceramic glazes and glassy coatings.

Keywords: Ceramic pigment; Colour; Crystal structure; Karrooite; Optical spectroscopy; Pseudobrookite

1. Introduction

A new field of application for karrooite, $MgTi_2O_5$, the magnesium end-term of the pseudobrookite series, is that of ceramic pigments. They are inorganic structures containing chromophore ions, which impart colour to ceramic wares by forming a heterogeneous mixture with the body or glaze in which they are dispersed [1]. In terms of requirements, ceramic pigments must be highly refractory, capable to withstand the chemical corrosion of liquid phases formed during the firing of bodies or glazes, and of suitable optical characteristics [1,2]. From this viewpoint, karrooite can be considered a potential ceramic pigment due to its refractoriness (melting point $\sim 1650\,^{\circ}C$) and high refractive indices ($n = 2.35$–2.42) though its stability is constrained by a strong thermal expansion anisotropy [3]. Moreover, it can host several transition metal ions in its octahedral coordination [4], thus enabling the development of different colours [5].

Karrooite is orthorhombic, space group *Bbmm*, whose structure consists of bands of edge-sharing octahedra extending in the *b* direction [6]. The cations are distributed over two crystallographically distinct and highly distorted octahedral sites: M_1 (4*c*) and M_2 (8*f*). M_1 is larger and more distorted than M_2. Each formula unit has one M_1 and two M_2 sites where Mg and Ti are accommodated with a certain degree of disorder. In the fully ordered structure, Mg is partitioned in M_1 and Ti in M_2; however, a wide range of non-convergent Mg/Ti order–disorder between M_1 and M_2 has been reported [7–9]. As well known, the cation ordering affects many physical properties of pseudobrookite-type compounds, e.g. structural changes [10], elasticity [11], high-temperature stabilization [12]. It may affect colour,

*Corresponding author. Present address: Tozzi Renewable Energy S.p.A., via Zuccherificio 10, 48010 Mezzano, Italy. Fax: +39 0546 46381.
E-mail address: francesco.matteucci@tozzisud.it (F. Matteucci).
[1]Present address: Centro Ceramico, Via Martelli 26, 40138 Bologna, Italy.

0022-4596/$ - see front matter © 2007 Elsevier Inc. All rights reserved.
doi:10.1016/j.jssc.2007.08.029

whenever the karrooite structure is doped with transition metals. In fact, chromophore ions are expected to undergo to a different crystal field strength in the two non-equivalent octahedral sites M_1 and M_2, due to the different metal–ligand distances and site distortion, implying significant changes in energy and intensity of optical bands [13].

The main goals of the present study are to understand the colouring mechanism of $MgTi_2O_5$ doped with several transition metals and to assess the potential of karrooite as ceramic pigment. The former aim was realized by coupling crystal structure determination with optical spectroscopy, while the latter was appraised through technological testing.

2. Experimental procedure

2.1. Sample preparation

Thirteen samples were prepared according to the stoichiometry: $Mg_{1-x}Ti_{2-x}M_{2x}O_5$, where $M = V$, Cr, Mn, Fe, Co, Ni, and $x = 0$, 0.02 and 0.05. They are named after the symbol and amount of dopant (e.g. $Mg_{0.98}Ti_{1.98}Cr_{0.04}O_5$ is named "Cr4") while the undoped karrooite ($MgTi_2O_5$) is referred to as "KT". Reagent-grade MgO, TiO_2, V_2O_5, Cr_2O_3, Mn_2O_3, Fe_2O_3, Co_3O_4, NiO were admixed and wet ground in a rotatory mill (5 min with de-ionized water and zirconia sintered balls). Mixtures were dried in oven (105 °C overnight) pulverized and put into alumina crucibles; firing was performed in an electric kiln with static air atmosphere, heating rate 200 °C per hour, maximum temperature 1300 °C, soaking time 4 h, natural cooling. Furthermore, ilmenite-type titanates $ATiO_3$ (where $A = Co$, Mg, Mn, Ni) were also synthesized with the same procedure for reference.

2.2. X-ray diffraction

Laboratory X-ray powder diffraction (XRD) was performed using a Philips PW1820/00 goniometer with graphite-monochromated Cu$K\alpha_{1,2}$ radiation (15–130° 2θ, 0.02° step-scan, 10 s per step).

The crystal structure refinements were performed using the Rietveld method with the GSAS and EXPGUI softwares [14,15]. Starting atomic parameters were taken from Yang and Hazen [8] for karrooite and from Liferovitch and Mitchell [16] for geikielite. Up to 49 independent variables were refined: scale-factors, zero-point, 10–15 coefficients of the shifted Chebyschev function to fit the background, unit cell dimensions, atomic positions, isotropic displacement parameters, profile coefficients (one Gaussian, G_W, two Lorentzian terms, L_x and L_y, and peak correction for asymmetry effects), preferred orientation along [001] of karrooite using March–Dollase approximation, octahedral site occupancies. Phase fractions and unit cell dimensions of accessory phases were refined too. The figures-of-merit of Rietveld refinements are listed in Table 1.

In particular, the occupancy parameter describing the Mg–Ti distribution was varied for each site keeping the total occupancy constrained to the stoichiometric value. It must be pointed out that, despite the relatively large contrast between the scattering factor of Mg^{2+} and Ti^{4+}, estimating the site occupancy fractions from XRD data is not free of errors. Furthermore, the refined titanium occupancy is actually the sum of Ti plus dopant, as the scattering factors of transition metals are closer to Ti than to Mg. The site distortion was evaluated considering both the octahedral angle variance ($OAV = \sigma_{\theta(oct)}$) and the octahedral quadratic elongation ($OQE = \lambda_{oct}$) [18].

2.3. Optical spectroscopy

Diffuse reflectance spectroscopy (DRS) was performed at room temperature with a Perkin-Elmer λ35 spectrophotometer in the 300–1100 nm range, 0.03 nm step size, using an integrating sphere and a white reference material, both made of $BaSO_4$. Reflectance (R_∞) was converted to

Table 1
Refinement parameters, phase composition and calculated solubility of chromophores in karrooite and geikielite

Sample	No. of variables	Figures-of-merit		Phase composition			Chromophore amount in karrooite (apfu)	Chromophore amount in geikielite (apfu)
		R_F^2	R_{wp}	$MgTi_2O_5$ (wt%)	$MgTiO_3$ (wt%)	TiO_2 (wt%)		
KT	49	0.06	0.18	96.9(3)	2.7(3)	0.4(1)	0.000	0.00
Co4	44	0.08	0.20	96.9(5)	3.1(3)	0.0(1)	0.035	0.24
Co10	44	0.06	0.18	87.9(3)	12.1(4)	0.0(1)	0.078	0.23
Cr4	47	0.07	0.18	98.2(2)	1.3(2)	0.5(1)	0.043	<0.01
Cr10	47	0.05	0.20	98.3(2)	1.2(3)	0.5(1)	0.101	<0.01
Fe4	44	0.06	0.19	96.5(3)	3.5(3)	0.0(1)	0.037	0.05
Fe10	45	0.08	0.27	98.2(4)	1.8(3)	0.0(1)	0.101	<0.01
Mn4	43	0.06	0.21	96.1(3)	3.9(3)	0.0(1)	0.039	0.06
Mn10	44	0.07	0.23	94.4(2)	5.6(4)	0.0(1)	0.098	0.13
Ni4	44	0.07	0.20	97.6(2)	2.4(4)	0.0(1)	0.038	<0.01
Ni10	33	0.07	0.23	92.3(2)	7.7(5)	0.0(1)	0.093	0.15
V4	39	0.10	0.25	98.3(3)	0.0(1)	1.7(2)	0.040	–
V10	47	0.07	0.22	93.6(4)	0.0(1)	6.4(3)	0.107	–

Notes: Figures in parentheses are standard deviations in the last decimal figure. R_F^2 is only referred to karrooite reflections.

absorbance (K/S) by the Kubelka–Munk equation: $K/S = 2(1-R_\infty) \times 2R_\infty^{-1}$ [19]. The positions of the main absorbance peaks in the optical spectra were determined through a deconvolution procedure (PFM, OriginLab) that allowed to obtain averaged values of crystal field strength Δ_o (by the Tanabe–Sugano diagrams and fitting spin-allowed transitions), band splitting δ (FWHM of the main optical band), crystal field stabilization energy CFSE (calculated by Δ_o values [13]), interelectronic repulsion Racah B parameter (by spin-allowed transitions [19–21]) and nephelauxetic ratio β (i.e. B/B_0, where B is experimental and B_0 is the value of the free ion) [20].

2.4. Colouring performance

Colour was measured by diffuse reflectance spectroscopy in the visible range (HunterLab Miniscan MSXP4000, 400–700 nm, D65 standard illuminant, 10° observer, white glazed tile reference $x = 31.5$, $y = 33.3$) and expressed in the CIE-Lab colour coordinates: L^* (100 = white, 0 = black), a^* (+red, −green), b^* (+yellow, −blue).

The technological behaviour was assessed for each chromophore on the sample that gave the best colour performance. Each pigment was added (5 wt%) into different ceramic glazes and glassy coatings that were fast fired in a roller kiln in industrial-like conditions. The chemical and physical characteristics of these ceramic coatings have been reported elsewhere [22].

3. Results

3.1. X-ray diffraction

The addition of transition metals induces significant changes in the phase composition, unit cell dimensions, ordering state, metal–oxygen distances and bond angles of $MgTi_2O_5$. Undoped karrooite exhibits values of cell parameters and cation ordering that are in between those of $MgTi_2O_5$ quenched at 800 and 1000 °C [10,23]. Therefore, it can be concluded that our natural cooling down from 1300 °C, performed in order to simulate the pigment manufacturing process, gave the same ordering state as quenching at approximately 900 °C.

3.1.1. Phase composition

The samples are not monophasic: a solid solution phase close to geikielite ($MgTiO_3$) is almost ubiquitous. It occurs together with rutile in KT and Cr-doped samples, while in the V-doped ones only rutile is found as accessory phase. Although in most cases the karrooite amount is over 95 wt%, the amount of accessory phase is not negligible in the samples Co10, Mn10, Ni10 and V10 (Table 1).

The geikielite unit cell parameters vary depending on the doping ion and amount. It was assumed, according to the Vegard's law, that the cell parameter variation along the $MgTiO_3$–$M TiO_3$ joint is linear, so that the amount of M (i.e. Co, Cr, Fe, Mn and Ni) in the solid solution may be estimated by the lever rule on the basis of the cell volumes of $MgTiO_3$ and the $M TiO_3$ end-member. This made it possible to calculate the transition metal solubilities in both karrooite and geikielite structures, with the former being fairly close to the expected amount of chromophore (Table 1).

3.1.2. Unit cell parameters

The variation of the unit cell edge lengths and volume in karrooite likely arises as a combination of two factors: (i) the different ionic size of doping ions and (ii) the order–disorder process among the two non-equivalent octahedral sites. In fact, while it is clear that a smaller ion substituting for a larger one will bring about a volume contraction, the same effect is also caused, with a fixed composition, for an increased degree of octahedral Mg/Ti ordering [6–8,23]. A more recent study of cation ordering in karrooite by neutron powder diffraction [38] confirmed that disorder leads to increased values for a, c and V but to a reduced b cell edge. The effect of Mg/Ti ordering will be discussed in a next section while the possible size effect is discussed here.

Doped karrooite samples exhibit significant structural changes that follow quite regular trends of the unit cell dimensions vs. the cell volume (Table 2). Exceptions are the V-doped karrooite having shorter a and longer b with respect to the general trend and the Cr- and Ni-doped samples, which have a longer c dimension (Fig. 1). Since disorder is expected to shorten the b-edge, the negative trend defined by V10, Fe10 and KT in Fig. 1 (middle) might be ascribed to this effect while the major positive trend (from Cr10 to Mn10) is more likely due to the size effect.

Overall, vanadium and chromium doping induced a contraction of the unit cell volume compared to the undoped karrooite; in contrast, an increased volume occurred in Mn-doped samples. Volume variations are small with Co, Fe and Ni doping (Fig. 1). Structural data of iron-bearing karrooite are consistent with those of armalcolite $Mg_{0.5}Fe_{0.5}Ti_2O_5$ [17,24].

For every transition metal, except the Mn-bearing samples, an inverse relationship between the doping amount and the unit cell volume can be observed (Table 2).

3.1.3. Variation of bond distances and order–disorder in octahedral sites

The distribution of Mg/Ti/dopant cations over the two non-equivalent octahedral sites can be first evaluated by a plot of $\langle M_1\text{–O} \rangle$ vs. $\langle M_2\text{–O} \rangle$ (Fig. 2) as compared with results from Yang and Hazen [8] and Lennie et al. [38]. Fig. 2 shows that, while our undoped karrooite sample ('KT') lies close to the structure with maximum degree of disorder reported by Ref. [8] ('Y&H-disord') and Ref. [38] ('K2'), most of the doped samples are distributed along a trend which is consistent with the 'Y&H-disord'-'Y&H-ord' and 'K2'–'K4' tielines. From this plot, it is clear that most of our doped karrooites are characterized by a

Table 2
Karrooite unit cell parameters, atomic displacements parameters and atomic positions

Sample	Unit cell parameters				Atomic displacement parameter, $U_{iso} \times 100$		Atomic positions			
	a (Å)	b (Å)	c (Å)	Volume (Å^3)	Cation	Anion	y(Mg,Ti)	x(O)	y(O)	z(O)
KT	9.7442(2)	9.9945(3)	3.74622)	364.84	2.0(1)	2.8(1)	0.2007(3)	0.2736(5)	0.3963(3)	0.4334(4)
Co4	9.7459(5)	9.9986(4)	3.7461(2)	365.04	3.0(1)	3.5(1)	0.2083(3)	0.2777(4)	0.3952(3)	0.4468(5)
Co10	9.7439(4)	10.0010(3)	3.7452(2)	364.96	2.7(1)	3.5(1)	0.2043(2)	0.2729(3)	0.3945(5)	0.4440(4)
Cr4	9.7407(3)	9.9887(4)	3.7480(1)	364.67	3.1(1)	3.5(1)	0.2011(3)	0.2671(3)	0.3958(4)	0.4317(5)
Cr10	9.7356(2)	9.9764(3)	3.7498(2)	364.21	2.7(1)	3.5(1)	0.2040(4)	0.2754(5)	0.3941(4)	0.4347(3)
Fe4	9.7470(3)	9.9970(3)	3.7465(1)	365.06	2.4(2)	2.7(1)	0.2022(4)	0.2745(5)	0.3873(3)	0.4357(4)
Fe10	9.7413(5)	9.9964(4)	3.7438(3)	364.56	2.8(3)	3.5(1)	0.2009(4)	0.2706(5)	0.3957(4)	0.4354(3)
Mn4	9.7440(5)	10.0034(7)	3.7456(2)	365.10	3.0(2)	3.5(1)	0.2058(4)	0.2745(7)	0.3839(5)	0.4443(7)
Mn10	9.7497(3)	10.0097(3)	3.7463(1)	365.61	2.3(2)	3.0(2)	0.2038(5)	0.2792(5)	0.3880(7)	0.4385(5)
Ni4	9.7442(3)	9.9917(3)	3.7480(2)	364.91	2.5(2)	2.9(3)	0.2011(4)	0.2760(4)	0.4023(4)	0.4379(6)
Ni10	9.7406(4)	9.9888(4)	3.7500(2)	364.86	2.8(3)	3.5(3)	0.2047(5)	0.2703(5)	0.3987(6)	0.4342(4)
V4	9.7301(5)	10.0061(5)	3.7445(4)	364.57	2.7(3)	3.5(3)	0.2015(6)	0.2706(6)	0.3976(4)	0.4428(6)
V10	9.7260(3)	10.0051(3)	3.7430(1)	364.23	3.0(2)	3.5(2)	0.2024(7)	0.2721(5)	0.3904(5)	0.4400(4)

Figures in parentheses are standard deviations in the last decimal figure.

larger degree of disorder compared to KT or Y&H-disord and K2. Exceptions to this behaviour are samples Mn4, Fe10, and V10 which show a noticeable degree of order.

Concerning the effect of order–disorder on the unit cell volume, a smaller value (363.53 Å^3) has been reported for the ordered form of undoped karrooite with respect to its more disordered form (365.00 Å^3) [8]. As previously noted (cf. Fig. 2), the cell volume contraction is actually accomplished by a lengthening of $\langle M_1$–O$\rangle$ accompanied by a shortening of $\langle M_2$–O$\rangle$. Such an inverse correlation also explains the anisotropic variation of the unit cell edge lengths. In the case of doped karrooite, the separation of size effect to the order–disorder effect is not a straightforward task. Samples Fe10, V10, Cr4, Cr10 and V4 show a smaller cell volume compared to undoped karrooite. Among those samples only for the first two the volume contraction could be ascribed to order–disorder effects.

Further insights into the octahedral ordering can be inferred from the occupancy refinement of M_1 site: the higher the Mg content in this larger site, the more ordered the Mg/Ti distribution. The refined Mg fraction is plotted vs. the difference of the average bond distances of the two octahedra relative to the grand mean distance (Fig. 3). The fraction of Mg at the M_1 site of undoped karrooite (0.65 for sample KT) is slightly larger than that reported by Ref. [8] although relatively close to the values found in other literature [25–26,38]. Considering the doped samples, the Mg fraction at M_1 appears to be overestimated too when compared to the trend defined by the 'Y&H' datapoints. Besides the uncertainty in the occupancy refinements, such an overestimation could be explained by the increased overall partitioning of Mg at M_1 induced by the dopant ions which, in turn, would be preferentially hosted at M_2. As an alternative interpretation, the creation of cation vacancies can be invoked to accommodate the substitution of Mg by doping ions with a charge greater than 2+. In fact, due to the full-occupancy constraint in the refinement, the lack of electron density at M_1 would lead to an (apparent) increase of the less-scattering species, Mg, at M_1.

In any case, Fig. 2 confirms that samples Mn4, Fe10 and V10 have an ordering pattern which is consistent to what was previously found in undoped karrooite.

3.1.4. Distortion of octahedral sites

The introduction of transition metals in the karrooite structure brought about a complex pattern of changes in the M–O distances and O–M–O bond angles with effects on the site distortion, here expressed by both the octahedral quadratic elongation OQE and octahedral angle variance OAV (Table 3).

The changes of M_1 and M_2 metal–oxygen distances can be associated to both the type and the amount of chromophore ions (Fig. 4). About the site M_1, the chromium and especially the cobalt doping provoked a shortening of $\langle M_1$–O$\rangle$, while V, Fe and Ni had little effect in small amount ($x = 0.02$) but caused an appreciable lengthening of the $\langle M_1$–O$\rangle$ distance once introduced in larger amount ($x = 0.05$); manganese doping exhibits an opposite effect, leading sample Mn4 to have a longer $\langle M_1$–O$\rangle$. These changes are to a large extent reversed in the site M_2, where Fe10, Mn4 and V10 have considerably shorter $\langle M_2$–O$\rangle$ lengths. All the other samples have longer metal–oxygen distances.

The doping caused an increase in the mean quadratic elongation at M_1 and a decreased distortion at M_2, but for the sample Fe10 (Fig. 4). At the same time, a diminution of the angle variance is systematically observed in both sites, except for Mn and V doping in M_1 (Fig. 5).

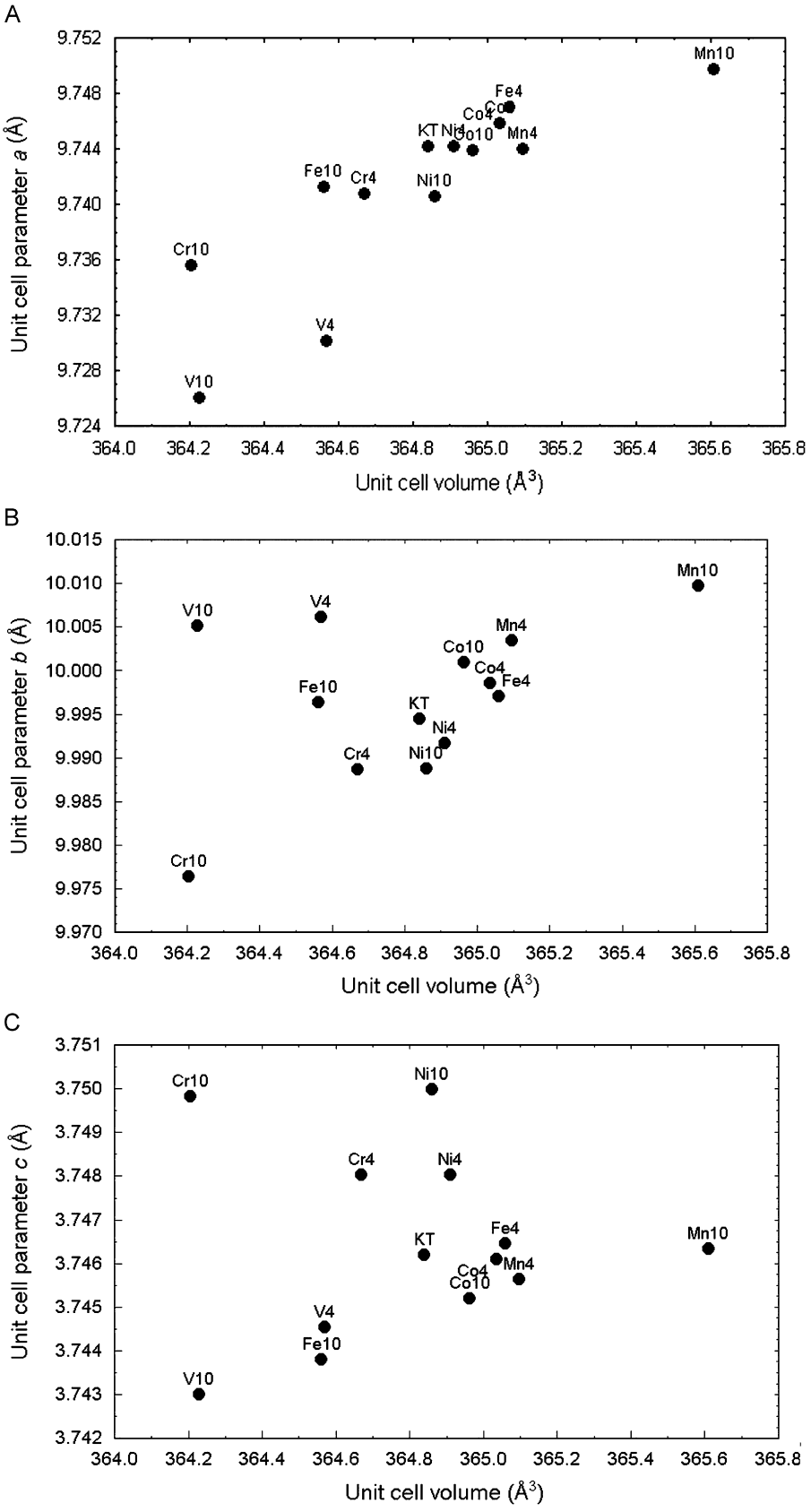

Fig. 1. Unit cell parameters vs. cell volume of karrooite samples.

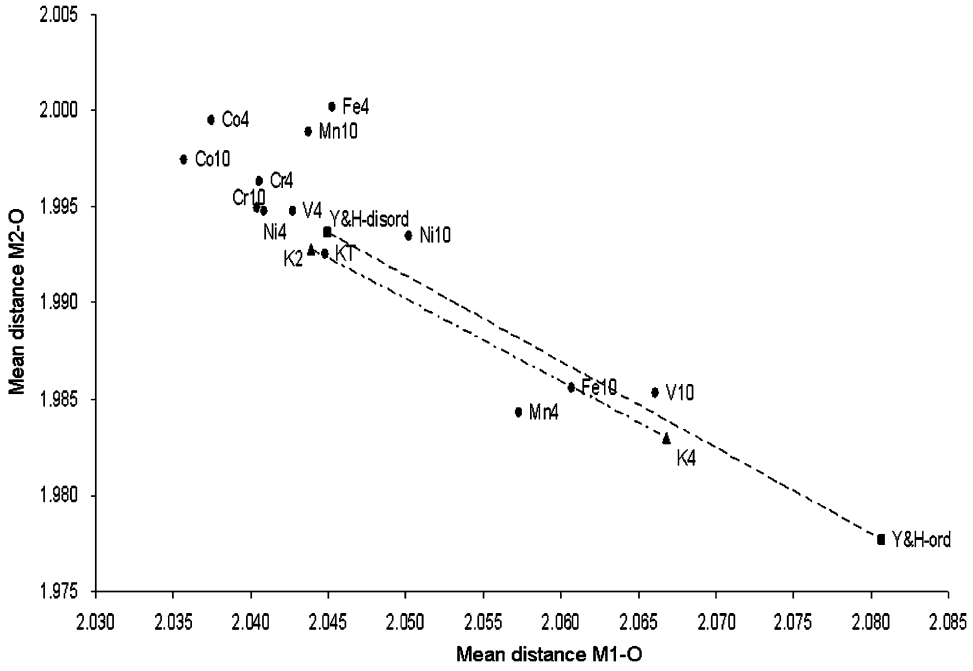

Fig. 2. Variation of $\langle M_2\text{–O}\rangle$ vs. $\langle M_1\text{–O}\rangle$. 'Y&H-disord', 'Y&H-ord' (squares and dashed line) are from Ref. [8] while 'K2' and 'K4' (triangles and dot-dash line) are room temperature data from Ref. [38].

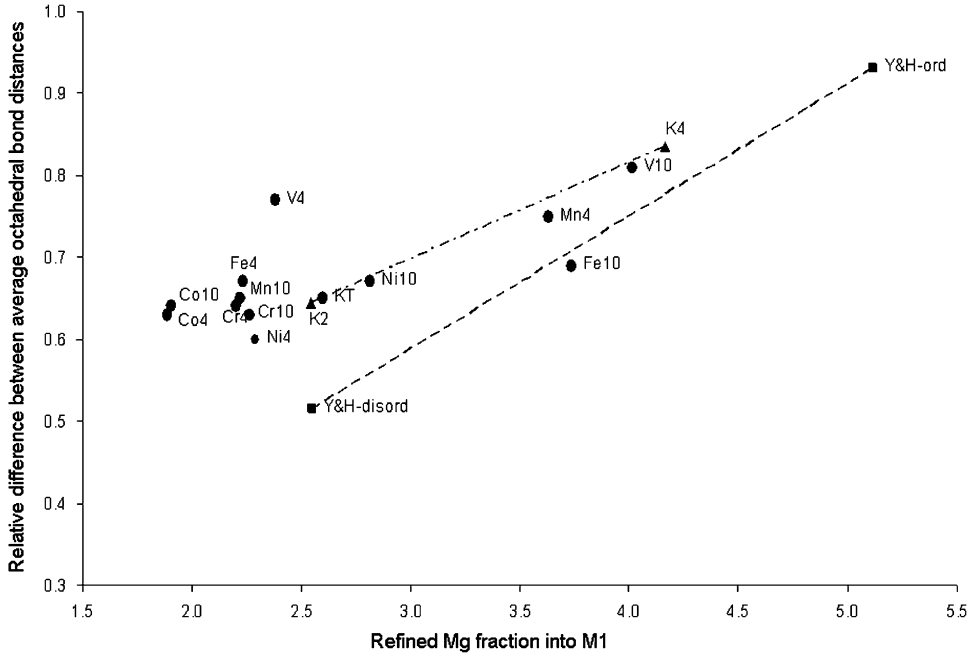

Fig. 3. Refined Mg fraction into M_1 (Mg fraction into M_2 is constrained to be equal to $[1-x_{Mg}]/2$) vs. the relative difference between average octahedral bond distances, Δ (%), calculated as $\Delta\,(\%) = 100\times(\langle M_1\text{–O}\rangle - \langle M_2\text{–O}\rangle)/[(\langle M_1\text{–O}\rangle + 2\times\langle M_2\text{–O}\rangle)/3]$. 'Y&H-disord', 'Y&H-ord' (squares and dashed line) are from Ref. [8] while 'K2' and 'K4' (triangles and dot-dash line) are room temperature data from Ref. [38].

Increasing the amount of dopant, from $x = 0.02$ to 0.05, brings about a drop of the octahedral angle variance in both sites with Ni and V doping, but a contemporary increase of the octahedral quadratic elongation in M_1 (Ni) or M_2 (V). In contrast, an obvious increase of both OAV and OQE occurs with Fe (site M_2) and Mn doping (site M_1). Doping with cobalt or chromium has little effect on site distortion.

3.2. Optical properties

The optical spectrum of undoped karrooite is characterized by a sharp band at ~30,000 cm^{-1}, probably due to the Ti^{4+}–O^{2-} charge transfer, by analogy with titania [19]. Being far in the UV, this band does not affect the colour, but in doped samples it overlaps some peaks of transition metals, making the interpretation more difficult. Therefore,

Table 3
Site occupancy and Mg–Ti ordering, average metal–oxygen distances, octahedral quadratic elongation and octahedral angle variance of karrooite

Sample	Site occupancy of Mg (apfu)		Average metal–oxygen distance (Å)		Octahedral quadratic elongation		Octahedral angle variance	
	M_1	M_2	M_1–O	M_2–O	M_1	M_2	M_1	M_2
KT	0.65	0.17	2.0448	1.9925	1.0014	1.0028	238.5	137.9
Co4	0.63	0.18	2.0375	1.9995	1.0021	1.0023	222.4	123.8
Co10	0.64	0.18	2.0357	1.9974	1.0018	1.0020	226.8	127.1
Cr4	0.64	0.18	2.0406	1.9963	1.0015	1.0025	214.3	122.1
Cr10	0.63	0.18	2.0404	1.9949	1.0016	1.0024	217.7	121.7
Fe4	0.67	0.17	2.0453	2.0002	1.0023	1.0024	226.0	112.7
Fe10	0.69	0.15	2.0607	1.9856	1.0012	1.0032	226.5	124.7
Mn4	0.75	0.13	2.0573	1.9843	1.0015	1.0020	244.0	135.0
Mn10	0.65	0.18	2.0437	1.9989	1.0024	1.0022	255.1	126.9
Ni4	0.60	0.20	2.0409	1.9948	1.0017	1.0025	231.9	129.9
Ni10	0.67	0.16	2.0502	1.9935	1.0025	1.0024	221.0	114.3
V4	0.77	0.11	2.0427	1.9948	1.0022	1.0020	252.2	123.8
V10	0.81	0.10	2.0661	1.9853	1.0021	1.0026	236.7	108.9

Standard deviation is (1) in the last decimal figure.

the karrooite contribution was systematically subtracted, so that optical spectra present an only apparent drop of absorbance at energies $>30{,}000\,cm^{-1}$. Spectral features do not change significantly by increasing doping for every transition metal; the most important fact is a strong increase of absorbance passing from $x=0.02$ to 0.05. Hence, the discussion of spectra will be the same for both loadings.

Discussing the relationships between crystal structural and spectroscopic data, any contribution from the accessory phase geikielite is neglected because it is considered to be to a large extent superimposed to that of karrooite. As a matter of fact, the site B of geikielite and the site M_2 of karrooite have almost the same M–O distance (i.e. 2.01 Å) and the latter plays a major role determining the crystal field strength.

3.2.1. Vanadium doping

The optical spectra of V-doped karrooite present a very wide hump absorbing intensely every wavelength over $20{,}000\,cm^{-1}$ and gently dipping toward IR. Two maxima of absorbance at ~23,000 and ~$27{,}000\,cm^{-1}$ and two shoulders in the 12,000–$15{,}000\,cm^{-1}$ range can be appreciated (Fig. 6). These spectra exhibit typical features of V(IV), e.g. the weak bands at ~12,000 and ~$15{,}000\,cm^{-1}$ that are observed also in other ceramic pigments containing V(IV), such as ZrO_2, $ZrSiO_4$ and $ZrTiO_4$ [27]. Besides its electronic configuration d^1, for which only a $t_{2g}^1 \rightarrow e_g^1$ transition is expected, the V(IV) ion gives rise—once in a distorted crystal site—to widely split transitions from the ground state ^2A_g to $^2B_{1g}$, $^2B_{2g}$, $^2B_{3g}$ and ^2A_g [28,29]. This splitting can explain the spectral features, taking into account a doubling of transitions due to the occurrence of V(IV) in both octahedral sites of karrooite (Fig. 6) with rather broad bands ($\delta = 3000$–$5000\,cm^{-1}$) for d–d transitions (Table 4). The crystal field strength is approximately 15,600 and $14{,}000\,cm^{-1}$ for M_1 and M_2 sites, respectively (Table 5). Though the presence of V(III) cannot be ruled out in such complex spectra, the clear separation of its main $^3T_{2g}$ and $^3T_{1g}$ transitions is missing.

3.2.2. Chromium doping

Cr-doped karrooite exhibits peculiar optical features: a strong absorbance all over the spectra with two distinct maxima at ~13,000 and ~$25{,}000\,cm^{-1}$, plus a shoulder at ~$19{,}000\,cm^{-1}$ (Fig. 7). These characteristics do not correspond to Cr(III) spectra [30], especially for the occurrence of an intense band below $15{,}000\,cm^{-1}$, being the minimum wavenumber of its $^4T_{2g}$ band $15{,}100\,cm^{-1}$ in the large octahedral site of zoisite [13]. Karrooite spectral features are attributable to Cr(IV) in octahedral coordination, where a d^2 ion has a t_{2g}^2 electronic configuration of the ground state $^3T_{1g}(^3F)$ and two main spin-allowed transitions to $t_{2g}^1 e_g^1$, i.e. $\nu_1 = {}^3T_{2g}(^3F)$ and $\nu_2 = {}^3T_{1g}(^3P)$; the further transition $\nu_3 = {}^3A_{2g}(^3F)$ is two electrons e_g^2, then less probable. The main band at ~$13{,}000\,cm^{-1}$ can be attributed to $^3T_{2g}$, the shoulder at ~$19{,}000\,cm^{-1}$ to $^3T_{1g}$ and the broad band at ~$25{,}000\,cm^{-1}$ to $^3A_{2g}$. A doubling of these transitions—due to the occurrence of Cr(IV) at both M_1 and M_2 sites—may account for the conspicuous peak broadening (Fig. 7; Table 4). This interpretation reasonably fits the Tanabe–Sugano diagram of d^2 ions, though peak energies are lower than expected and the intensity of the $^3A_{2g}$ band too high. The corresponding Δ_o values are ~22,000 (M_1) and ~$19{,}000\,cm^{-1}$ (M_2) for Racah B ~600 (M_1) and ~$500\,cm^{-1}$ (M_2) so implying a possible difference in the covalent degree of Cr–O bonding in M_2 (Table 5). ν_1 is alternatively interpreted as the spin-forbidden $^1T_{2g}$ (^1G), $\nu_2 = {}^3T_{2g}$ and $\nu_3 = {}^3T_{1g}$, as in titanate pyrochlores [31,32], but in this case ν_2 would not fit the Tanabe–Sugano diagram and some special effect would be invoked to account for the strong intensity of $^1T_{2g}$.

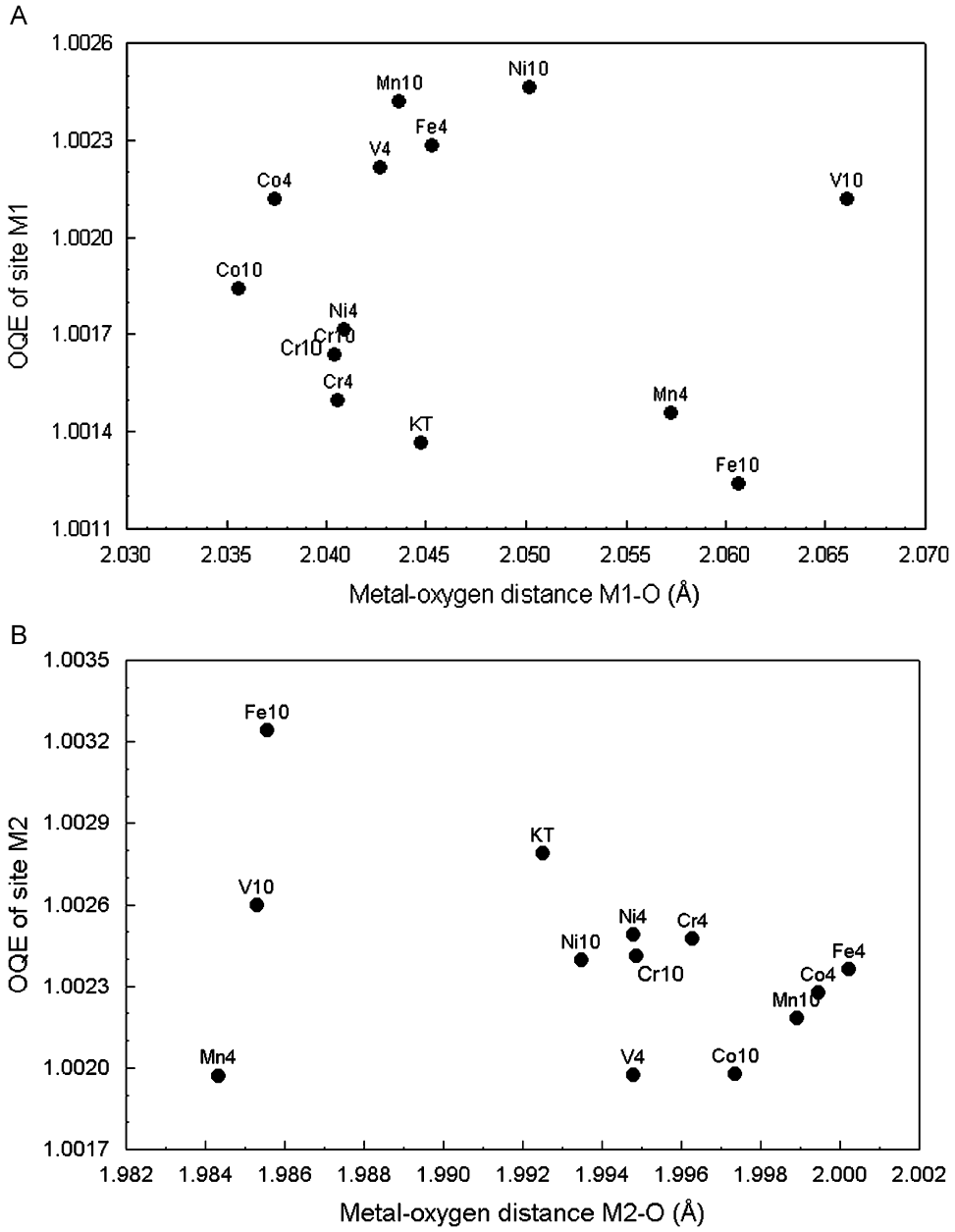

Fig. 4. Mean metal–oxygen distance vs. octahedral quadratic elongation (OQE) of the site M_1 (above) and M_2 (below) of karrooite.

3.2.3. Manganese doping

The occurrence of manganese causes a strong absorbance in the high-energy part of the spectrum with a maximum at ~24,000 cm^{-1} and two shoulders around 12,000 and 18,000 cm^{-1} (Fig. 8). These complex spectra are due to complementary contributions from both Mn(II) and Mn(III) ions: the former gives four intense bands mostly over 20,000 cm^{-1}, while the latter undergoes a splitting in three bands usually below 22,000 cm^{-1} [19,20]. This situation implies the occurrence of seven bands, so it was not possible to further distinguish distinct contribution from pyrophanite ($MnTiO_3$) or the M_1 and M_2 sites of karrooite (Table 4). The three-fold split transition $^5E_g(^5D) \rightarrow {}^5T_2(^5D)$ of Mn(III) accounts for the broad spectral components (FWHM 4000–5000 cm^{-1}) at ~10,000, ~16,000 and ~21,000 cm^{-1} (Fig. 8). Resulting spectroscopic parameters, Δ_o ~13,000 cm^{-1} and Racah B ~900 cm^{-1} (Table 5), are close to those of piemontite $Ca_2(Al,Mn,Fe)_3(SiO_4)_3(OH)$, where Mn(III) occurs in the M_3 site, that is larger and more distorted than M_2 site of karrooite [33]. Being a d^5 ion, Mn(II) has only spin-forbidden transitions from the ground state $^6A_1(^6S)$ to $^4T_1$, $^4T_2$ and $^4E,{}^4A(^4G)$, $^4T_2$ and $^4E(^3D)$. The correspondent bands fit the Tanabe–Sugano diagram for Δ_o ~8500 cm^{-1} and Racah B ~800 cm^{-1}, which is remarkably higher than in the known Mn(II) spectra [13,20].

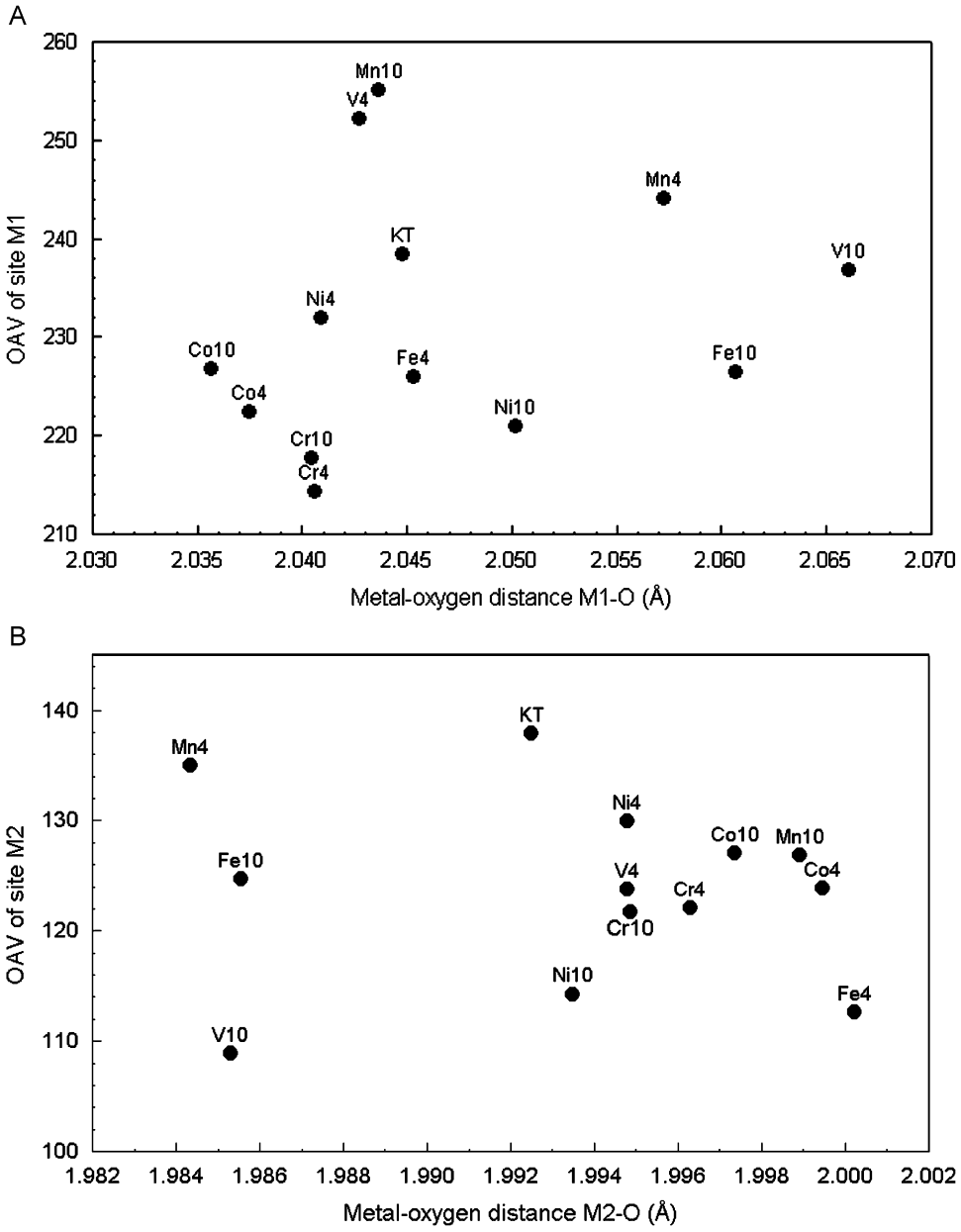

Fig. 5. Mean metal–oxygen distance vs. octahedral angle variance (OAV) of the site M_1 (above) and M_2 (below) of karrooite.

3.2.4. Iron doping

Iron-bearing karrooite pigments present a typical optical spectrum of Fe(III), characterized by a strong absorbance in the near UV, with additional bands clearly appreciable at ~21,000 and ~24,000 cm^{-1} plus weak contributions at lower energies (Fig. 9). In the Fe(III) spectra, the bands at higher energies (i.e. $>20{,}000\,cm^{-1}$) are due to spin-forbidden transitions between the ground state $^6A_1(^6S)$, having a $t_{2g}^3e_{2g}^2$ electronic configuration, and excited states with the same $t_{2g}^3e_{2g}^2$ configuration such as $^4E,^4A(^4G)$ at ~21,000 cm^{-1} or ^4E and $^4T_2(^4D)$, merging at ~24,000 cm^{-1} and partially overlapped by the Fe–O charge transfer accounting for the strong band in the near UV [18–20]. In the low-energy part of the spectrum, there are weak bands originating from spin-forbidden transitions to $^4T_1$ and $^4T_2(^4G)$ states with $t_{2g}^4e_{2g}^1$ configuration (Table 4). Spectra were deconvolved considering a doubling of the $^4T_1$ and $^4T_2$ transitions—the only to be dependent on the crystal field in d^5 ions—due to the occurrence of Fe(III) at both sites of karrooite (Fig. 9). Results fit satisfactorily the Tanabe–Sugano diagram with Δ_o ~14,000 (M_1) and ~11,500 cm^{-1} (M_2) for Racah B ~700 cm^{-1} (Table 5) that is higher than in known Fe(III) oxides, particularly the isostructural pseudobrookite [34]. This correspondence is less convincing for the ^4E and $^4T_2(^4D)$ transitions, probably because of the interference by the Fe–O charge transfer.

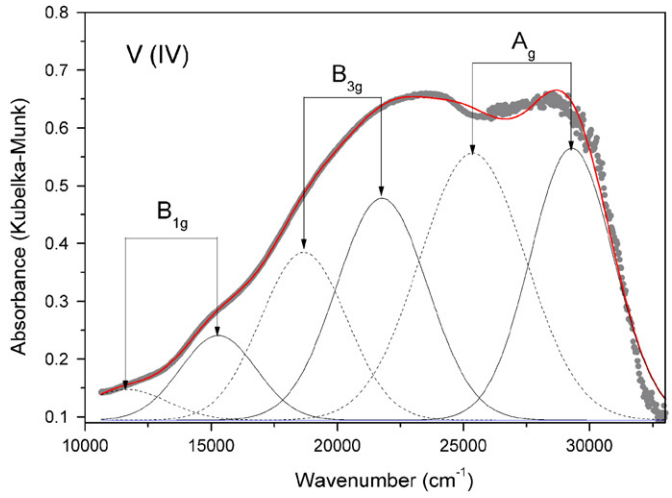

Fig. 6. Diffuse reflectance spectrum of sample V10 with deconvolution of optical bands.

3.2.5. Cobalt doping

The optical spectra of Co-bearing karrooite exhibit distinct features: a huge hump centred at ~25,000 cm^{-1}, a sharp band at ~16,000 cm^{-1} with a weaker one at ~13,000 cm^{-1}, plus the tail of a peak with its maximum <9000 cm^{-1} (Fig. 10). The spectra can be interpreted with *d–d* transitions of Co(II) in octahedral environment and by a Co–O charge transfer accounting for the hump over 25,000 cm^{-1} (Fig. 10). Co(II) is a d^7 ion with a $t_{2g}^5e_{2g}^2$ electronic configuration of its ground excited states $^4T_{2g}(^4F)$, $^4A_{2g}(^4F)$ and $^4T_{1g}(^4P)$ corresponding to the $t_{2g}^4e_g^3$, $t_{2g}^3e_g^4$ and $t_{2g}^5e_g^2$ configurations, respectively. Being a two-electrons transition, $^4A_{2g}$ is expected to be much less intense than the other two [13,20,35]. The spectra were deconvolved admitting a doubling of the $^4A_{2g}$ and $^4T_{1g}$ transitions, due to the presence of Co ions at both octahedral sites of karrooite, which are referred to the bands at ~13,000 and ~16,000 cm^{-1}, respectively

Table 4
Optical spectroscopic data of Co-, Cr-, Fe-, Mn-, Ni- and V-doped karrooite

	Electronic transition	Site	Doping $x = 0.02$ apfu			Doping $x = 0.05$ apfu		
			Peak (cm^{-1})	δ (cm^{-1})	Area (a.u.)	Peak (cm^{-1})	δ (cm^{-1})	Area (a.u.)
Co(II)	$^4T_{1g}(^4F)\rightarrow{}^4A_{2g}(^4F)$	M_1	13,810	1630	60	13,480	1990	200
		M_2	12,660	1410	50	12,260	1520	130
	$^4T_{1g}(^4F)\rightarrow{}^4T_{1g}(^4P)$	M_1	18,250	2560	470	17,600	2810	1260
		M_2	16,710	2280	570	16,480	1840	550
	$^4T_{1g}(^4F)\rightarrow{}^2A_{1g}(^2G)$	Both	22,660	3840	530	22,690	5570	1220
Cr(IV)	$^3T_{1g}(^3F)\rightarrow{}^3T_{2g}(^3F)$	M_1	14,620	4020	1400	14,470	4020	2150
		M_2	11,990	5000	1450	12,040	5000	2170
	$^3T_{1g}(^3F)\rightarrow{}^3T_{1g}(^3P)$	M_1	21,500	3520	1160	20,700	3610	1430
		M_2	18,870	3520	1050	18,520	3320	1430
	$^3T_{1g}(^3F)\rightarrow{}^3A_{2g}(^3F)$	M_1	28,900	4290	2880	28,750	4840	4170
		M_2	25,010	4590	3050	24,240	4920	4930
Fe(III)	$^6A_1(^6S)\rightarrow{}^4T_1(^4G)$	M_1	14,420	4340	350	14,420	4310	460
		M_2	11,840	4970	280	11,410	4310	350
	$^6A_1(^6S)\rightarrow{}^4T_2(^4G)$	M_1	18,200	3040	310	18,080	2850	470
		M_2	16,160	3650	320	15,860	3270	340
	$^6A_1(^6S)\rightarrow{}^4E,{}^4A(^4G)$	Both	20,870	3570	510	20,600	2790	760
	$^6A_1(^6S)\rightarrow{}^4E,{}^4T_2(^4D)$	Both	24,820	4420	830	24,380	4690	2340
Mn(II)	$^6A_1(^6S)\rightarrow{}^4T_1(^4G)$	Both	18,900	3970	1390	17,490	3860	2420
	$^6A_1\rightarrow{}^4T_2(^4G)$	Both	24,200	3370	1990	23,720	4310	4280
	$^6A_1\rightarrow{}^4E,{}^4A(^4G)$	Both	26,860	3290	1990	26,970	3760	2860
	$^6A_1\rightarrow{}^4E,{}^4T_2(^4D)$	Both	29,630	3270	1790	29,760	3410	2150
Mn(III)	$^5E_g(^5D)\rightarrow{}^5T_2(^5D)$							
	d_{xz}, d_{yz}	Both	10,730	5000	1060	10,130	5000	2300
	$d_{x^2-y^2}$	Both	16,110	4280	890	14,610	4490	2200
	d_{z2}	Both	21,640	3680	1880	20,440	3980	3120
Ni(II)	$^3A_{2g}(^3F)\rightarrow{}^3T_{1g}(^3F)$	M_1	13,520	3840	410	13,640	2090	420
		M_2	11,750	3440	340	11,800	3200	930
	$^3A_{2g}(^3F)\rightarrow{}^1T_{2g}(^1D)$	M_1	19,350	2260	130	19,310	1650	250
		M_2	17,640	2440	100	17,920	1510	80
	$^3A_{2g}(^3F)\rightarrow{}^3T_{1g}(^3P)$	M_1	22,880	2900	430	22,950	2640	830
		M_2	21,260	2660	380	21,220	2640	860
	$^3A_{2g}(^3F)\rightarrow{}^1T_{1g}(^1G)$	Both	25,750	2250	250	25,390	2180	460
V(IV)	$^2A_g(^2D)\rightarrow{}^2B_{1g},{}^2B_{2g}(^2D)$	M_1	15,280	3560	550	14,470	3490	1610
		M_2	11,650	3840	160	11,400	2970	710
	$^2A_g(^2D)\rightarrow{}^2B_{3g}(^2D)$	M_1	21,770	4240	1730	20,940	4560	3790

Table 4 (*continued*)

Electronic transition	Site	Doping $x = 0.02$ apfu			Doping $x = 0.05$ apfu		
		Peak (cm^{-1})	δ (cm^{-1})	Area (a.u.)	Peak (cm^{-1})	δ (cm^{-1})	Area (a.u.)
$^2A_g(^2D) \rightarrow {}^2A_g(^2D)$	M_2	18,670	4010	1240	17,780	4030	2630
	M_1	29,300	3860	1910	29,080	4370	3290
	M_2	25,370	4930	2430	24,800	5000	4560

Table 5
Crystal field strength (Δ_o), crystal field stabilization energy (CFSE), interelectronic repulsion Racah B parameter and nephelauxetic ratio $\beta = B/B_0$ (B_0 is the value of the free ion)

Sample	Dopant	Site M_1				Site M_2			
		Δ_o (cm^{-1})	CFSE (kJ g/ion)	B (cm^{-1})	β (adimensional)	Δ_o (cm^{-1})	CFSE (kJ g/ion)	B (cm^{-1})	β (adimensional)
Co4	Co(II)	7220	−69.1	830	0.85	6620	−63.4	760	0.78
Co10		7060	−67.6	795	0.82	6420	−61.5	755	0.78
Cr4	Cr(IV)	22240	−212.9	595	0.57	19510	−186.8	500	0.48
Cr10		21400	−204.9	635	0.61	19160	−183.4	470	0.45
Fe4	Fe(III)	13850	0	703	0.71	11390	0	703	0.71
Fe10		14700	0	694	0.70	11460	0	694	0.70
Ni4	Ni(II)	9310	−133.7	665	0.64	8080	−116.0	682	0.66
Ni10		9370	−134.5	665	0.64	8110	−116.5	676	0.65
V4	V(IV)	15650	−74.9	–	–	14120	−67.6	–	–
V10		15590	−74.6	–	–	13370	−64.0	–	–

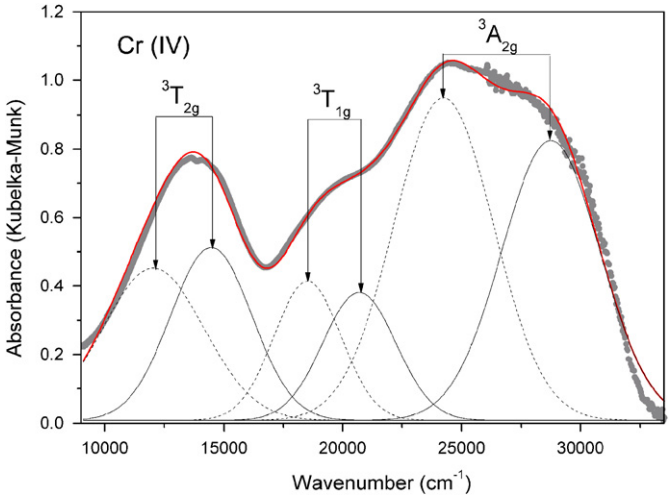

Fig. 7. Diffuse reflectance spectrum of sample Cr10 with deconvolution of optical bands.

(Table 4), attributing the tail of the peak centred $<9000\,cm^{-1}$ to the transition $^4T_{2g}$. This is in good agreement with the Tanabe–Sugano diagram, resulting in Δ_o ~7100 (M_1) and ~6500 cm^{-1} (M_2) with Racah B close to 800 cm^{-1} (Table 5). The hump at high energy, however, cannot be successfully deconvolved without taking into account a weak contribution at ~22,500 cm^{-1}, which may be attributed to the spin-forbidden transition $^2A_{1g}$ [18,35].

3.2.6. Nickel doping

The optical spectra of Ni-bearing karrooite exhibit three clearly appreciable absorbance bands (Fig. 11): one in the near infrared (~13,000 cm^{-1}), one in the blue (~22,000 cm^{-1}) and one in the UV (~28,000 cm^{-1}), with a shoulder in the green (~19,000 cm^{-1}). These features match the effects of Ni(II) in octahedral field plus an important contribution by a Ni–O charge transfer in the near UV. Ni(II) is a d^8 ion with a ground state $^3A_{2g}(^3F)$ and $t_{2g}^6e_g^2$ electronic configuration, which brings about three spin-allowed transitions: $^3T_{2g}(^3F)$ and $^3T_{1g}(^3F)$ to the $t_{2g}^5e_g^3$ configuration and the two-electrons $^3T_{1g}(^3P)$ to the $t_{2g}^4e_g^4$; besides, several weaker spin-forbidden transitions are possible as well [20,36]. According to this picture, spectra were deconvolved using eight bands for the *d–d* transitions, implying a doubling of the spin-allowed ones related to the occurrence of Ni(II) at both crystal sites of karrooite (Table 4). The main bands at ~13,000 and ~22,000 cm^{-1} were attributed to $^3T_{1g}(^3F)$ and $^3T_{1g}(^3P)$, respectively; a tail of the $^3T_{2g}$ is probably contributing below 10,000 cm^{-1} (Fig. 11). This is in accordance with the Tanabe–Sugano diagram, implying Δ_o as high as ~9300 (M_1) and ~8100 cm^{-1} (M_2) for a Racah B ~670 cm^{-1} (Table 5). The shoulder at ~22,000 $cm^{-1}$is

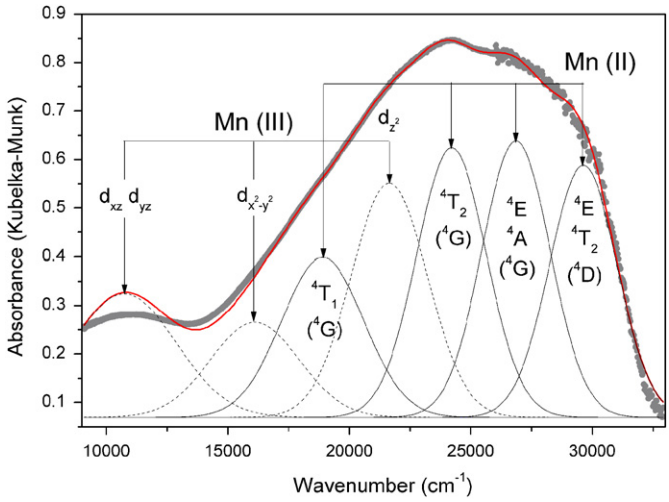

Fig. 8. Diffuse reflectance spectrum of sample Mn10 with deconvolution of optical bands.

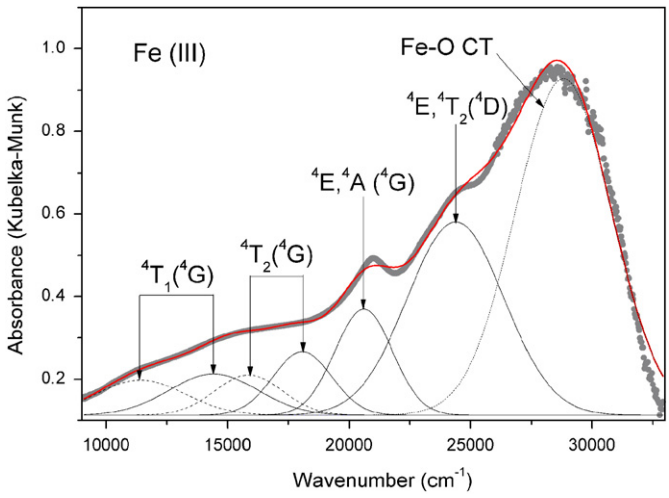

Fig. 9. Diffuse reflectance spectrum of sample Fe10 with deconvolution of optical bands.

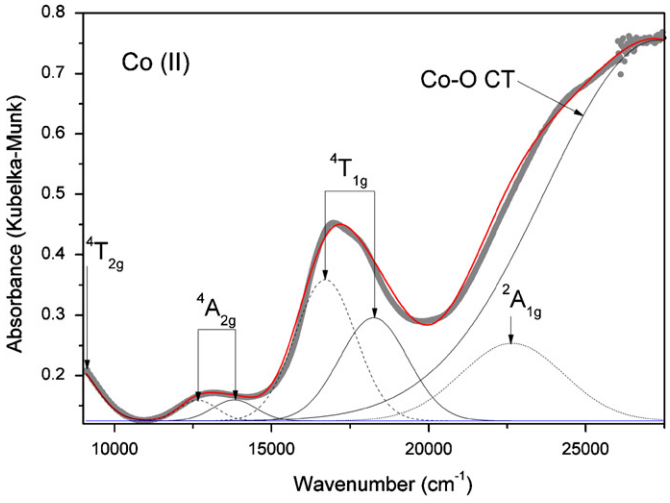

Fig. 10. Diffuse reflectance spectrum of sample Co10 with deconvolution of optical bands.

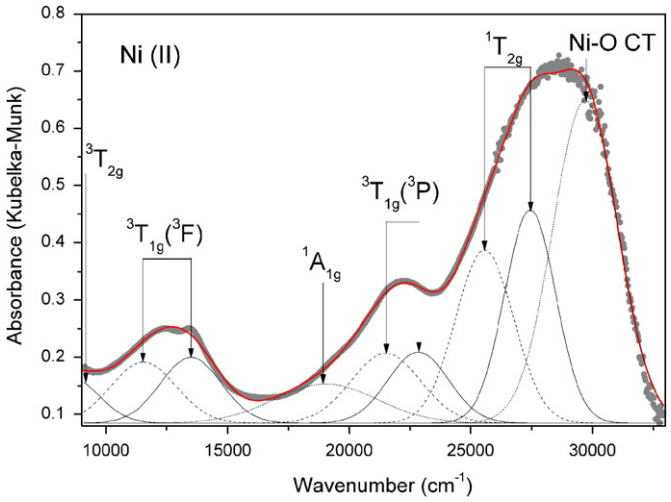

Fig. 11. Diffuse reflectance spectrum of sample Ni10 with deconvolution of optical bands.

Table 6
CIE Lab colourimetric parameters of karrooite pigments

Sample	L^*	a^*	b^*
Co4	56.4	−7.1	15.2
Co10	44.8	−6.2	11.9
Cr4	56.4	−5.8	12.0
Cr10	53.4	4.2	25.3
Fe4	44.8	−6.2	11.9
Fe10	66.0	0.8	18.6
Mn4	59.8	3.0	23.9
Mn10	34.8	5.9	13.9
Ni4	60.3	1.1	20.7
Ni10	73.7	8.1	39.8
V4	53.4	4.2	25.3
V10	38.3	13.1	16.0

tentatively related to the spin-forbidden transition $^1A_{1g}(^1G)$.

3.3. Colouring performance

The colourimetric parameters of karrooite pigments are summarized in Table 6. The V-doped karrooite reflects the light essentially in the red-yellow window, so justifying, together with the strong absorbance in the visible range, being orange-brown colour. The chromium doping induces a maximum reflectance around 16,000 cm^{-1}, giving rise to an orange shade with a fair purity of colour, especially for the sample Cr10. In the case of manganese addition, the maximum reflectance is at the red-IR border (~13,500 cm^{-1}) resulting in a brown colour with a more or less evident red cast. The iron-bearing karrooite has a wide reflectance window in the red-green region, so that its colour is brown-tan with a low purity or even with a green overtone in the sample Fe4, due to a further reflectance contribution at ~19,500 cm^{-1}. Two reflectance windows, a

stronger in the red ($\sim$15,000 cm^{-1}) and a less intense in the green ($\sim$20,000 cm^{-1}), make the Co-doped karrooite to be greenish, because the human eye is more sensitive to these wavelengths; a yellow cast is due to the complete absorption of the blue-violet component, while the red radiation dirties the green shade, so lowering colour purity. In the Ni-doped karrooite, a strong reflectance at $\sim$16,500 cm^{-1} justifies the yellow shade with a certain orange cast.

The behaviour of karrooite pigments in ceramic glazes and glassy coatings is shown in Fig. 12. Their colouring performance is kept, or even significantly improved in the case of Cr and Mn dopings, in glassy coatings fired up to 1000 °C. Once dispersed in ceramic glazes, karrooite pigments exhibit a progressive colour change with increasing temperature, implying a loss of both colour saturation (increasing L^*) and chroma (decreasing a^* and b^*). Such behaviour is likely related to chemical attack which karrooite undergoes by the aggressive liquid phase developed by glazes over 1100 °C, causing a gradual leaching of chromophores that dissolve into the glass imparting light brown (Cr, Fe, Mn, Ni and V) or light blue (Co) shades.

4. Discussion

The doping of karrooite caused a complex pattern of structural changes, involving metal–oxygen distances, tetragonal and trigonal distortion of octahedral sites, and Mg–Ti ordering. Along with some general trends, occurring to most samples with very few exceptions, there are specific situations for each dopant.

With respect to undoped karrooite, whose unit cell volume is consistent with a highly disordered state of the octahedral cations, doping induced a net contraction of the unit cell volume in five karrooite samples (V10, V4, Cr10, Cr4, Fe10) while a cell expansion took place in the other seven samples. The effect in the first group of samples can be explained by a combination of an enhanced octahedral ordering (V10, Fe10) and the smaller ionic size of dopants. For the remaining samples, except Mn4, both the cell volume increase and the difference between the two non-equivalent octahedral bond distances suggest that doping promotes disordering of octahedral cations (including Mg and Ti) among the M_1 and M_2 sites.

In general, no obvious correlations appear to exist between the observed order–disorder behaviour and the increase in tetragonal elongation of M_1 site and decrease of M_2 site distortion which occurred, as a whole, in doped karrooites.

In terms of the ionic radii [37] variation with respect to Mg(II) (0.72 Å) and Ti(IV) (0.605 Å), it can be noted that V(IV) (0.58 Å) is the smallest ion while the other dopants have an ionic size comprised between that of Mg and Ti. Thus, it is not surprising that V(IV) promotes more significant structural variations (order–disorder and site distortion) while the other ions have a less conspicuous effect with an increasing trend in the series $Cr < Ni \cong Co$ which is somewhat consistent with ionic radii.

In details, doping with Co, Cr and V gave a uniform pattern of metal–oxygen distances, site distortion and Mg–Ti ordering. Both cobalt and chromium doping had little effect on order–disorder, reduced the M–O lengths at the site M_1, making it more tetragonally elongated, and increased the M–O distances at the site M_2, rendering it less distorted. Even if a preference of Co(II) and Cr(IV) for the site M_1, being tetragonally distorted, is expected on the basis of CFSE considerations [13], optical data indicate a disordered distribution of such cations in the two octahedral sites of karrooite. The vanadium doping causes a remarkable ordering, associated with both M–O mean distance and distortion, which are increased at site M_1 and decreased at site M_2. The occurrence of V(IV) would imply a preference for the more trigonally distorted site, i.e. M_2, which is consistent with both ordering (more Mg in the site M_1) and M–O length. On other hand, Fe-, Mn- and Ni-doped samples also exhibit a dependence on the amount of dopant, giving often contrasting results. Anyway, no preference for the octahedral sites is expected on the basis of size or distortion, as Fe(III) and Mn(II) have no CFSE, and Ni(II) has a CFSE independent on site geometry [13].

The disordered distribution of transition elements in the karrooite lattice has an important effect on optical properties. Since the two octahedral sites are significantly different for their mean M–O distances and tetragonal or trigonal distortion, the same cation shall undergo a stronger crystal field interaction at M_1 than at M_2. In fact, distinct optical contributions from a chromophore ion at M_1 and M_2 have been recognized for every dopant but manganese. The correspondent Δ_o values are consistent with the crystal field theory expectations for the mean M_1–O and M_2–O distances [13,19,21]. Thus optical spectra are characterized by two sets of electronic absorption lines, slightly shifting each other, due to the chromophore occurrence at both octahedral sites of karrooite. As a consequence, optical bands are broad and their light absorption much less selective than in high-performance pigments, resulting in a low purity of colour.

5. Conclusions

Karrooite can easily accommodate transition elements of the first row into its crystal structure, but in industrial-like synthesis conditions their solubility is limited: additions of as high as 0.1 apfu bring about the formation of up to 10 wt% accessory phases (geikielite and/or rutile).

A relatively complex variation of the unit cell parameters in doped karrooites results from the interplay of two different factors: (i) the different ionic size of doping ions and (ii) the octahedral ordering.

Doping with Co, Cr, Fe, Mn, Ni or V induced a complex structural rearrangement of karrooite crystal lattice, involving Mg–Ti ordering as well as metal–oxygen bond

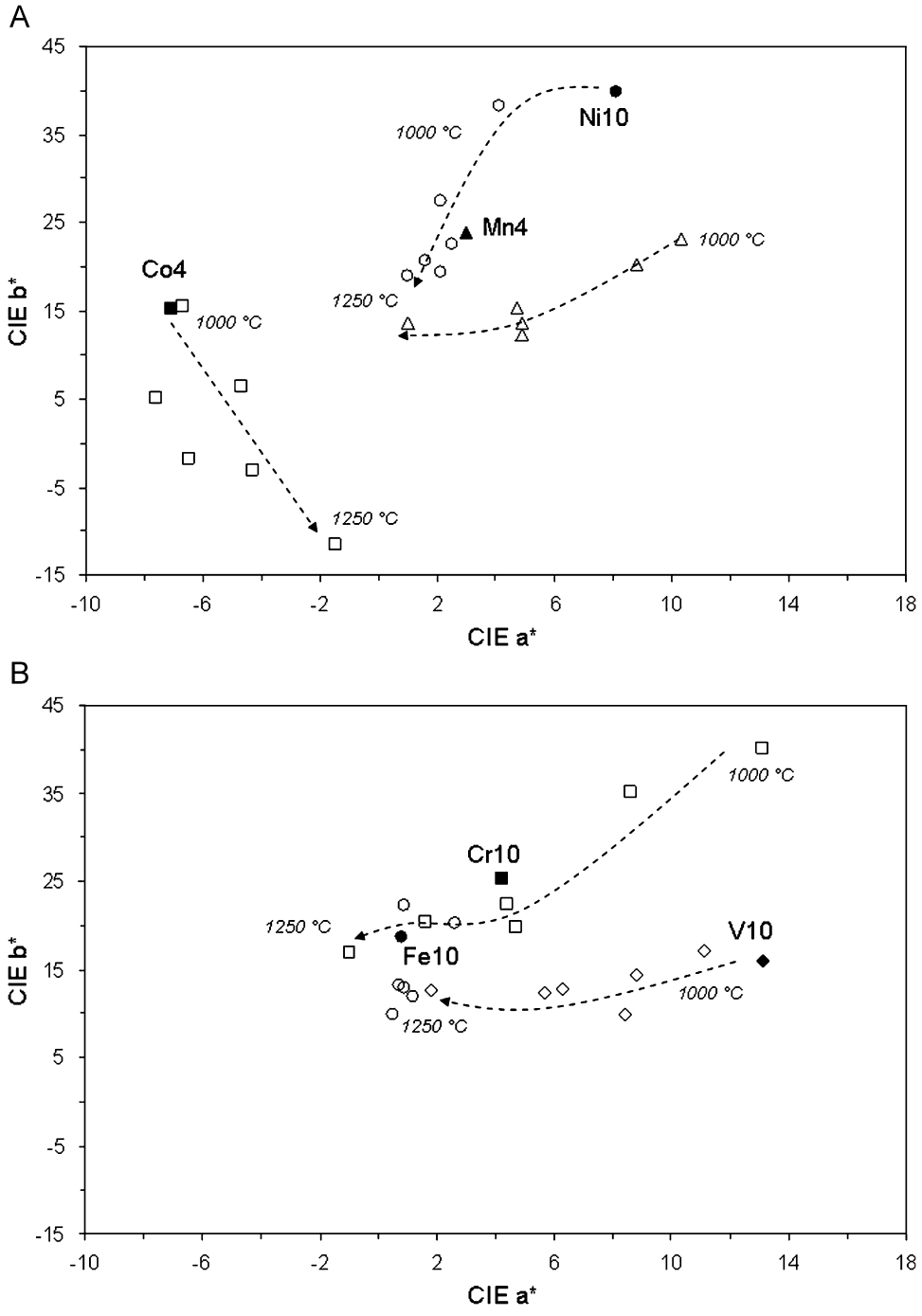

Fig. 12. Colour plot of karrooite pigments applied in ceramic glazes and glassy coatings fired from 1000 to 1250 °C. (A) Co-, Mn- and Ni-doped samples. (B) Cr-, Fe- and V-doped samples.

lengths and angles. Transition elements are hosted at both the octahedral sites with no apparent ordering, but for vanadium that seems to be preferentially allocated at site M_2.

Optical spectra are characterized by broad bands due to distinct contributions from Co(II), Cr(IV), Fe(III), Ni(II) or V(IV) at both M_1 and M_2 sites. Manganese appears in both (II) and (III) valencies. Crystal structural (metal–oxygen mean distance) and optical data (Δ_o) match to a large extent the predictions of the crystal field theory.

The resulting absorption of visible light is poorly selective and gives rise to low purity colours: orange-buff (Cr and V), brown-tan (Fe and Mn), yellow (Ni) and green (Co). Karrooite applied as ceramic pigment is stable in glassy coatings for firing temperatures of $<1050\,^{\circ}C$.

References

[1] R.A. Eppler, in: R.E. Kirk, D.F. Othmer (Eds.), Encyclopedia of Chemical Technology, vol. 6, Interscience, New York, 1993, p. 877.

[2] A.L. Costa, G. Cruciani, M. Dondi, F. Matteucci, Ind. Ceram. 23 (2003) 1–11.
[3] G. Bayer, J. Less-Common Met. 24 (1971) 129–138.
[4] D. Xirouchakis, A. Smirnov, K. Woody, D.H. Lindsley, D.J. Andersen, Am. Mineral. 87 (2002) 658–667.
[5] G. Blasse, G.J. Dirksen, Chem. Phys. Lett. 77 (1981) 9–11.
[6] B.A. Wechsler, A. Navrotsky, J. Solid State Chem. 55 (1984) 165–180.
[7] B.A. Wechsler, R.B. Von Dreele, Acta Crystallogr. B 45 (1989) 542–549.
[8] H. Yang, R.M. Hazen, Am. Mineral. 84 (1999) 130–137.
[9] M.S. Ghiorso, H. Yang, R.M. Hazen, Am. Mineral. 84 (1999) 1370–1374.
[10] H. Yang, R.M. Hazen, J. Solid State Chem. 138 (1998) 238–244.
[11] R.M. Hazen, H. Yang, Science 277 (1997) 1965–1967.
[12] A. Navrotsky, Am. Mineral. 60 (1975) 249–256.
[13] R.G. Burns, Mineralogical Applications of Crystal Field Theory, second ed., Cambridge University Press, Cambridge, 1993.
[14] A.C. Larson, R.B. Von Dreele, Los Alamos National Laboratory Report LAUR, 2000, pp. 86–748.
[15] H. Toby, J. Appl. Cryst. 34 (2001) 210–213.
[16] R.P. Liferovitch, R.H. Mitchell, Acta Crystallogr. B 60 (2004) 496–501.
[17] M.D. Lind, R.M. Housley, Science 175 (1972) 521–523.
[18] K. Robinson, G.V. Gibbs, P.H. Ribbe, Science 172 (1971) 567–570.
[19] S. Marfunin, Physics of Minerals and Inorganic Materials, Springer, Berlin, Heidelberg, New York, 1979.
[20] A.B.P. Lever, Inorganic Electronic Spectroscopy, Amsterdam, Elsevier, 1984.
[21] M. Wildner, M. Andrut, C.Z. Rudowicz, in: A. Beran, E. Libowitzky (Eds.), Optical Absorption Spectroscopy in Geosciences, Part I: Basic Concepts of Crystal Field Theory, EMU Notes in Mineralogy, vol. 6, Eotvos University Press, 2004, p. 93.
[22] F. Matteucci, C. Lepri Neto, M. Dondi, G. Cruciani, G. Baldi, A.O. Boschi, Adv. Appl. Ceram. 105 (2) (2006) 99–106.
[23] N.E. Brown, A. Navrotsky, Am. Mineral. 74 (1989) 902–912.
[24] B.A. Wechsler, Am. Mineral. 62 (1977) 913–920.
[25] R.G. Teller, M.R. Antonio, A.E. Grau, M. Gueguin, E. Kostiner, J. Solid State Chem. 88 (1990) 334–350.
[26] E. Grey, C. Li, I.C. Madsen, J. Solid State Chem. 113 (1994) 62–73.
[27] M. Dondi, F. Matteucci, G. Cruciani, J. Solid State Chem. 179 (2006) 233–246.
[28] A. Niesert, M. Hanrath, A. Siggel, M. Jansen, K. Langer, J. Solid State Chem. 169 (2002) 6–12.
[29] M. Dondi, F. Matteucci, I. Zama, G. Cruciani, Mater. Res. Bull. 42 (2007) 64–79.
[30] R.S. Pavlov, V.B. Marzá, J.B. Carda, J. Mater. Chem. 12 (2002) 2825–2832.
[31] F. Matteucci, G. Cruciani, M. Dondi, G. Baldi, A. Barzanti, Acta Mater. 55 (2007) 2229–2238.
[32] E. López-Navarrete, V.M. Orera, F.J. Lázaro, J.B. Carda, M. Ocaña, J. Am. Ceram. Soc. 87 (11) (2004) 2108–2113.
[33] R.G. Burns, R.G.J. Strens, Mineral. Mag. 36 (1967) 204–226.
[34] M. Dondi, F. Matteucci, G. Cruciani, G. Gasparotto, D.M. Tobaldi, Solid State Sci. 9 (2007) 362–369.
[35] M. Wildner, K. Langer, Phys. Chem. Miner. 20 (1994) 460–468.
[36] X. Hu, K. Langer, D. Boström, Eur. J. Mineral. 2 (1990) 29–41.
[37] R.D. Shannon, Acta Crystallogr. A 32 (1976) 751–767.
[38] A.R. Lennie, K.S. Knight, C.M.B. Henderson, Am. Mineral. 92 (2007) 1165–1180.